Ab Initio Trajectory Study on Triplet Ketene Photodissociation via Statistical Sampling of the Crossing Seam

Yusuke Ogihara, Takeshi Yamamoto,* and Shigeki Kato

Department of Chemistry, Kyoto University, Kyoto 606-8502, Japan

ABSTRACT: Triplet ketene exhibits a steplike structure in the experimentally observed dissociation rate, but its mechanism is still unclear despite many theoretical efforts. A previous surface-hopping simulation at the CASSCF level suggests that nonadiabatic transition from the S_0 to T_1 states creates the T_1 species in a highly nonstatistical manner, which raises the question of whether the use of statistical rate theory is valid in itself for the T_1 state. Here, we study this problem by performing ab initio trajectory simulation at the multireference second-order Möller−Plesset perturbation (MRMP) level of theory. Since the MRMP theory is too expensive for such a trajectory calculation, we first construct dual-level potential energy surfaces (PESs) for the S_0 and T_1 states by calibrating the PESs at the B3LYP level with a limited set of MRMP energies. We then introduce the assumption of vibrational equilibrium on the S_0 surface and characterize the $S_0 \rightarrow T_1$ crossing points using the conditional microcanonical distribution on the S_0/T_1 seam surface. The latter distribution is obtained by running a constrained trajectory on the seam surface by use of an efficient SHAKE-like method. Subsequently, we propagate a number of T_1 trajectories from the seam surface to obtain the dissociation rate. The result shows that (i) the $S_0 \rightarrow T_1$ crossing points are localized mainly in the T_1 reactant region; (ii) the lifetime on the T_1 surface is about 30 ps at the MRMP level, which is 2 orders of magnitude greater than the previous estimate obtained from the surface-hopping simulation at the CASSCF level ($\sim$100 fs); and (iii) the calculated T_1 dissociation rate agrees reasonably well with classical transition state theory. These results suggest that the T_1 dissociation is rather statistical, given that the T_1 trajectories are initiated from the conditional microcanonical distribution on the seam surface.

I. INTRODUCTION

In the early 1990s, Kim et al.[1,2] performed an experimental study on the photodissociation of triplet ketene, $CH_2CO \rightarrow CH_2 + CO$. In their experiment, the ketene molecule in the S_0 state was first excited to the S_1 state via a UV laser, and the excited ketene underwent nonadiabatic transition to lower electronic states, followed by intersystem crossing from S_0 to T_1 states; see Figure 1 for a schematic of relevant potential energy surfaces (PESs). An interesting observation here is that the dissociation rate of triplet ketene, $k(E)$, exhibits a steplike structure as a function of total energy E near the dissociation threshold. The steplike structure in $k(E)$ was interpreted as arising from vibrationally quantized states at the transition state (TS). On the basis of this interpretation, the observed steps in $k(E)$ were discussed in terms of energy levels of vibrational modes orthogonal to the reaction coordinate, and semiquantitative agreement was obtained between the width of the observed steps and the level spacing of orthogonal modes at the transition state.[2]

However, a subsequent quantum dynamical study by Gezelter and Miller[3] demonstrated that if one takes into account tunneling effects along the reaction coordinate, the steps in $k(E)$ should be eliminated (or "washed out") by tunneling, which results in a nearly structureless profile of $k(E)$. The situation can be described more clearly by considering the microcanonical rate expression for unimolecular dissociation:[4,5]

$$k(E) = \frac{N(E)}{2\pi\hbar\rho(E)} \quad (1)$$

where $N(E)$ is the cumulative reaction probability (CRP) and $\rho(E)$ is the density of reactant states. For the present system, the CRP can be approximated accurately as follows:[6]

$$N(E) \approx \sum_i \kappa(E - E_i^{\ddagger}) \quad (2)$$

where $E_i^{\ddagger}$ is the energy of the ith vibrational level at the TS and $\kappa(E)$ is the one-dimensional transmission probability calculated along the reaction coordinate. In the classical limit, $\kappa(E)$ reverts to the Heaviside step function, $\kappa(E - E_i^{\ddagger}) \rightarrow \Theta(E - E_i^{\ddagger})$, and the $N(E)$ always exhibits a steplike structure. In the quantum case, $\kappa(E - E_i^{\ddagger})$ increases gradually from 0 to 1 when passing $E = E_i^{\ddagger}$, and if the width of $\kappa(E - E_i^{\ddagger})$ is greater than the level spacing $E_i^{\ddagger} - E_{i-1}^{\ddagger}$, one can no longer observe a steplike structure in $N(E)$. By utilizing the accurate PES at the CCSD level obtained by Schaefer and co-workers,[7] Gezelter et al. demonstrated that the width of $\kappa(E - E_i^{\ddagger})$ is actually much greater than the spacing of energy levels $E_i^{\ddagger} - E_{i-1}^{\ddagger}$, resulting in a structureless profile of $k(E)$. They also suggested that in order for the steps to appear in $k(E)$, the imaginary frequency $\omega^{\ddagger}$ at the TS needs to be less than $\sim$100 cm^{-1}, which is 3−4 times smaller than the result at the CCSD level (379 cm^{-1}).[7] Recently, we have also carried out an ab initio calculation of triplet ketene at the multireference levels of theory,[6,8] but the obtained $\omega^{\ddagger}$ was about 300 cm^{-1}, and thus the steps in $k(E)$ were not reproduced. Here, it is worth noting that a similar discrepancy exists between theory and experiment for the photodissociation of triplet acetaldehyde.[9,10] In the latter
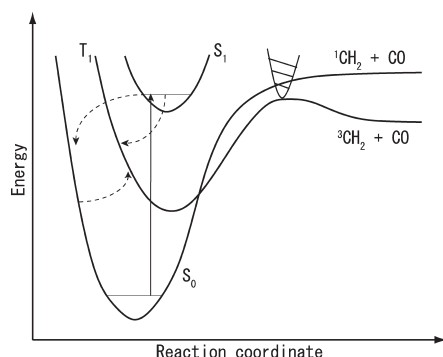
Figure 1. A schematic of S_0, S_1, and T_1 potential energy surfaces of triplet ketene. Dashed arrows indicate possible pathways of nonadiabatic transition. In this paper, we assume that the molecule reaches a vibrational equilibrium on the S_0 surface prior to the intersystem crossing to the T_1 surface. The direct $S_1 \rightarrow T_1$ pathway is neglected throughout this paper.

Figure 2. Transition state geometry of triplet ketene. R is the CC bond length, θ is the CCO bending angle, and ϕ is the torsional angle.

case, the imaginary frequency estimated from the experiment is 60 cm^{-1}, whereas accurate quantum-chemical calculations predict $300-500 \text{ cm}^{-1}$.

As such, possible mechanisms other than vibrational quantization at the TS were also explored for explaining the observed steps. Cui and Morokuma performed an extensive ab initio study on nonadiabatic interactions among the relevant PESs.[11] Their study suggested that $S_1 \rightarrow S_0$ internal conversion is very efficient, while the direct $S_1 \rightarrow T_1$ pathway is negligible due to the extremely small spin—orbit coupling as well as the high location of the S_1/T_1 minimum seam crossing (MSX) point. As a result, they concluded that $S_1 \rightarrow S_0 \rightarrow T_1$ is the dominant pathway for the triplet dissociation. Subsequently, Kaledin et al.[12] performed a direct surface-hopping trajectory calculation at the state-averaged (SA) CASSCF level. They propagated a trajectory, starting at the Franck—Condon geometry on S_1, and branched it out into many child trajectories every time the propagating PES crossed with another PES. Their calculation suggested that (1) the S_0-T_1 nonadiabatic transition creates the T_1 species non-statistically at restricted regions of phase space and (2) a large fraction of the T_1 species thus created dissociates almost immediately (within 120 fs), thus leaving no time for equilibration on the T_1 surface. Those observations suggest that the dissociation dynamics on the T_1 surface are highly nonstatistical, which raises the question of whether equilibrium-based rate theories [such as eq 1] are valid in themselves for describing the T_1 dissociation.

It should be pointed out, however, that the surface-hopping simulation by Kaledin et al.[12] was not without limitation (which is essentially due to the limited computational power available in 2001). First, they utilized the CASSCF method to describe the S_0 and T_1 surfaces, but in fact the latter method is not very accurate for describing the dissociation profile (see section II.A). Specifically, the dissociation barrier height on the T_1 surface is predicted to be 16 kcal/mol at the CASSCF level, while that at the multireference level of theory is 29 kcal/mol. The significantly smaller barrier height at the CASSCF level may be partly responsible for the fast dissociation observed in ref 12. Second, the surface-hopping simulation was performed with the "ant" method.[13,14] However, the relatively small number of propagated trajectories (about 10) makes it difficult to assess the statistical significance of the results, particularly considering that the $S_0 \rightarrow T_1$ transition
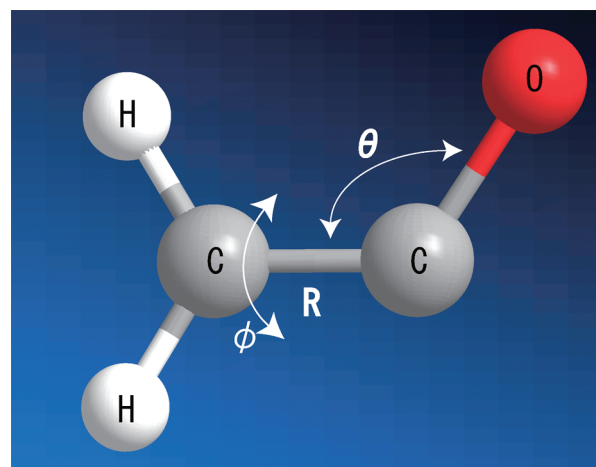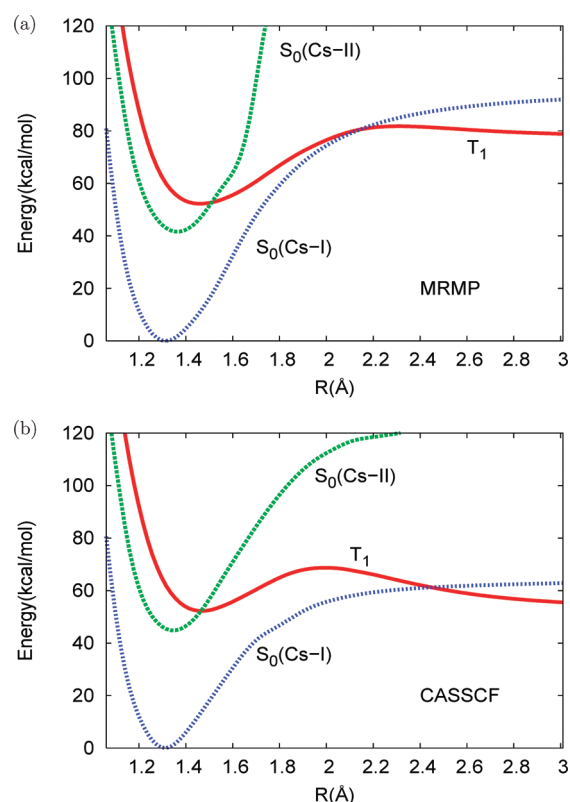

Figure 3. Minimum energy profiles of the S_0 and T_1 surfaces obtained with (a) MRMP and (b) CASSCF methods. Internal coordinates other than R are optimized at each value of R. The minimum energy path on the S_0 surface is of nonplanar Cs—I symmetry, while that on the T_1 surface is of planar Cs—II symmetry. The green line with label "S_0-(Cs—II)" represents the S_0 potential energy curve calculated along the T_1 minimum energy path.

probability is very small (on the order of 10^{-5}).[12] Third, the trajectory calculation was performed in planar Cs—II symmetry with the torsional angle ϕ set at zero (see Figure 2). This is based on the observation that all of the important geometries (including the S_0/T_1 MSX point) belong to planar Cs—II symmetry. However, the minimum energy profile on the S_0 surface is known to be of

nonplanar Cs—I symmetry,[7] and therefore it is desirable that no restriction on ϕ is applied in the trajectory calculation.

The purpose of this paper is thus to perform an ab initio trajectory calculation of triplet ketene by lifting some of the limitations mentioned above, while describing the relevant PESs more accurately with the multireference second-order Möller—Plesset perturbation (MRMP) theory. Specifically, we first construct dual-level PESs for the S_0 and T_1 states by combining the accuracy of the MRMP theory and the efficiency of the B3LYP method (section II.A). We then introduce the assumption of vibrational equilibrium on the S_0 surface and characterize the $S_0 \rightarrow T_1$ crossing points using the conditional microcanonical distribution on the S_0/T_1 seam surface (section II.B). The latter distribution is obtained by running a constrained trajectory on the seam surface via use of an efficient SHAKE-like method.[15,16] Subsequently, we propagate a number of T_1 trajectories starting from the seam distribution thus obtained and calculate the dissociation rate on the T_1 surface. We emphasize that the present study does not make the assumption of vibrational equilibrium on the T_1 surface; rather, we assume that the molecule reaches a vibrational equilibrium on the S_0 surface prior to $S_0 \rightarrow T_1$ intersystem crossing. As such, comparison of the present trajectory result with statistical rate theory (based on a vibrational equilibrium on the T_1 surface) provides useful insight into the statistical degree of the T_1 dissociation (section III.B).

II. METHOD

II.A. Construction of Dual-Level Potential Energy Surfaces. To perform an ab initio trajectory calculation, one needs to select an appropriate level of electronic structure theory that is not too expensive yet provides a sufficient accuracy for the relevant PESs. To do so, we first compare in Figure 3 several one-dimensional potential profiles calculated at the CASSCF and MRMP levels. Here, both the CASSCF and MRMP calculations were performed with the cc-pVTZ basis set,[17] and the active space was constructed by distributing 14 electrons in 11 molecular orbitals. The minimum energy profiles of the S_0 and T_1 states in Figure 3 are obtained from energy minimization at fixed R. As noted above, the reaction path on the T_1 surface is of planar Cs—II symmetry, while that on the S_0 surface is of nonplanar Cs—I symmetry. Figure 3 also displays the S_0 potential energy profile calculated along the T_1 reaction path, which crosses the T_1 minimum energy profile at around $R = 1.5$ Å. This is consistent with the fact the S_0/T_1 MSX point is located near the T_1 minimum geometry.[11] The dissociation barrier height on the T_1 surface is calculated to be 16.3 and 29.3 kcal/mol at the CASSCF and MRMP levels, respectively. The MRMP result is in excellent agreement with the T_1 barrier height at the UCCSD(T) level[7] (29.8 kcal/mol), while the CASSCF result is significantly smaller than the MRMP or UCCSD(T) result. This fact underlines the importance of dynamic electron correlation in the TS region.[6] Furthermore, we compare in Figure 4 the minimum energy profiles obtained at the (U)B3LYP/6-31G* level with the CASSCF and MRMP results. We see that the B3LYP method gives a rather accurate PES for the S_0 state, whereas it is less accurate for the T_1 state.

In the following, we construct an approximate dual-level PES in order to combine the accuracy of the MRMP theory and the efficiency of the B3LYP method. (For previous applications of this type of method, see refs 18 and 19, for example.) Here, we choose the CC bond length R as the reaction coordinate and
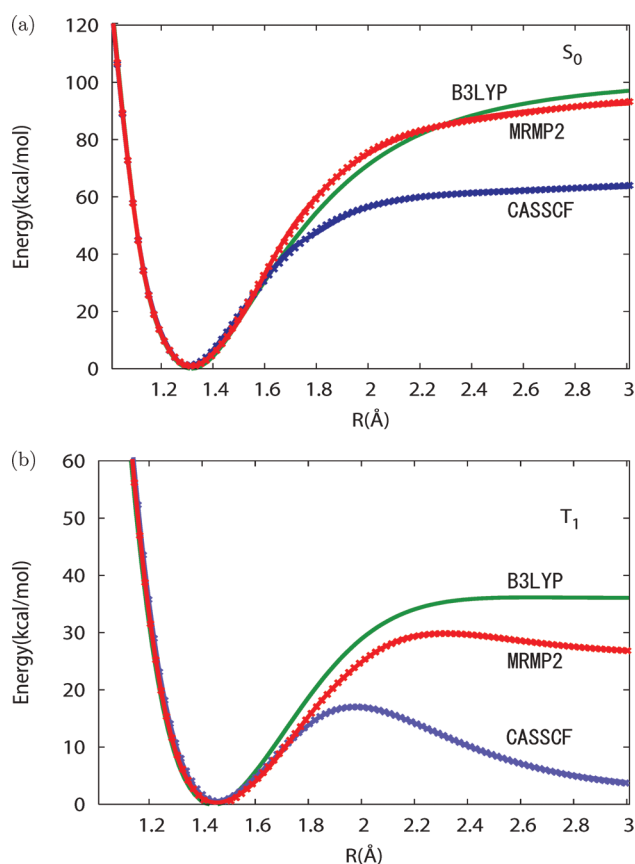

Figure 4. Minimum energy profiles calculated at the MRMP, CASSCF, and B3LYP levels (solid line): (a) S_0 state, (b) T_1 state. Minimum energy profiles of the MRMP::B3LYP and CASSCF::B3LYP potential functions are plotted with cross symbols, which agree almost exactly with the underlying MRMP and CASSCF ones.

consider the functional form

$$U_{DL}(\mathbf{r}) = U_{LL}(\mathbf{r}) + U_{HL}^{min}(R) - U_{LL}^{min}(R) \qquad (3)$$

Here, $\mathbf{r}$ is the Cartesian coordinates of the molecule and $U_{HL}^{min}(R)$ and $U_{LL}^{min}(R)$ are the minimum energy profiles of high- and low-level potential functions denoted as $U_{HL}(\mathbf{r})$ and $U_{LL}(\mathbf{r})$. We suppose that the latter are calculated with the MRMP and B3LYP methods, respectively. The minimum energy profiles of $U_{HL}(\mathbf{r})$ and $U_{LL}(\mathbf{r})$ are defined here as

$$U_{LL}^{min}(R) = \min_{\mathbf{q}} U_{LL}(R, \mathbf{q}) \qquad (4a)$$

$$U_{HL}^{min}(R) = \min_{\mathbf{q}} U_{HL}(R, \mathbf{q}) \qquad (4b)$$

where $\mathbf{q}$ denotes the internal coordinates other than R. $U_{LL}^{min}(R)$ and $U_{HL}^{min}(R)$ are obtained from energy minimization at fixed R. The minimum energy profiles are then fit analytically with the following function:

$$U_{HL}^{min}(R) - U_{LL}^{min}(R) \simeq \Delta U_\infty \left\{ 1 - \sum_{k=1}^{4} c_k \exp[-(R - R_k)^k] \right\}$$

$$(5)$$

where $\{c_k\}$ and $\{R_k\}$ are adjustable parameters obtained from a least-squares fit. ΔU_∞ represents the energy difference of the

products between the high- and low-level theories. Due to the definition in eq 3, the minimum energy profile of the dual-level PES coincides exactly with that of the high-level PES, i.e.,

$$\min_{\mathbf{q}} U_{DL}(\mathbf{r}) = U_{HL}^{min}(R) \tag{6}$$

This property ensures the good accuracy of the dual-level PES in the vicinity of the minimum energy path. On the other hand, the accuracy of $U_{DL}(\mathbf{r})$ in the direction of $\mathbf{q}$ is determined by the low-level theory [see eq 3]. Since the B3LYP method often provides a good description of bound degrees of freedom, we expect that $U_{DL}(\mathbf{r})$ also behaves reasonably well as a function of $\mathbf{q}$ (see below for numerical tests). The stationary points on the dual-level PES are determined by the condition

$$\frac{\partial U_{DL}(R, \mathbf{q})}{\partial R} = 0 \tag{7a}$$

$$\frac{\partial U_{DL}(R, \mathbf{q})}{\partial \mathbf{q}} = \frac{\partial U_{LL}(R, \mathbf{q})}{\partial \mathbf{q}} = 0 \tag{7b}$$

The second equation gives the optimized value of $\mathbf{q}$ as a function of R, which will be denoted as $\mathbf{q}_*(R)$. The latter is obtained by minimizing the low-level potential at fixed R. Insertion of $\mathbf{q}_*(R)$ into the first equation gives

$$\frac{\partial U_{DL}(R, \mathbf{q}_*(R))}{\partial R} = \frac{dU_{HL}^{min}(R)}{dR} = 0 \tag{8}$$

which states that the stationary value of R coincides with that of the minimum energy profile of the high-level PES. As for the Hessian matrix of the dual-level PES, we have

$$\frac{\partial^2 U_{DL}(R, \mathbf{q})}{\partial R^2} = \frac{\partial^2 U_{LL}(R, \mathbf{q})}{\partial R^2} + \frac{\partial^2 U_c(R)}{\partial R^2} \tag{9a}$$

$$\frac{\partial^2 U_{DL}(R, \mathbf{q})}{\partial R \partial \mathbf{q}} = \frac{\partial^2 U_{LL}(R, \mathbf{q})}{\partial R \partial \mathbf{q}} \tag{9b}$$

$$\frac{\partial^2 U_{DL}(R, \mathbf{q})}{\partial \mathbf{q} \partial \mathbf{q}} = \frac{\partial^2 U_{LL}(R, \mathbf{q})}{\partial \mathbf{q} \partial \mathbf{q}} \tag{9c}$$

with $U_c(R) = U_{HL}^{min}(R) - U_{LL}^{min}(R)$. The Hessian matrix is thus largely determined by the low-level theory, while the element in the direction of R is determined by the high-level theory.

Hereafter, we will denote the dual-level potential function thus obtained as MRMP2::B3LYP, where a pair of high- and low-level theories are denoted with double colons. For comparison, we also constructed a dual-level CASSCF::B3LYP potential function. We calculated high-level potential energies using the GAMESS program package,[20] while low-level energies are calculated with the Firefly package.[21] This is because the Firefly package provides a significant acceleration of computational speed (typically by a factor of 4) over the standard GAMESS program for the B3LYP method. To construct the MRMP::B3LYP PES, we calculated the minimum energy profile $U_{HL}^{min}(R)$ approximately using the minimum energy path at the CASSCF level. This is because analytical gradients for the MRMP method are not available in the GAMESS program.[20] We emphasize, however, that the property in eq 6 holds even if we calculate $U_{HL}^{min}(R)$ approximately.

We now assess the accuracy of the dual-level potential functions thus obtained. First, we display in Figure 4 the

Table 1. Equilibrium Geometry on the S_0 Surface[a]

	MRMP(DL)	CASSCF(DL)	CASSCF
CC	1.312	1.307	1.309
CH_1	1.084	1.084	1.073
CH_2	1.084	1.084	1.073
CO	1.176	1.176	1.164
∠HCH	120.0	120.0	120.0
∠HCC	120.0	120.0	120.0
∠CCO	180.0	180.0	180.0

[a] MRMP(DL) and CASSCF(DL) stand for the dual-level MRMP::B3LYP and CASSCF::B3LYP potential functions, respectively. Bond lengths are in Ångstroms, and angles are in degrees.

Table 2. Equilibrium and TS Geometries on the T_1 Surface[a]

	MRMP(DL)	MRMP[a]	CASSCF(DL)	CASSCF
		equilibrium geometry		
CC	1.463	1.461	1.470	1.466
CH_1	1.089	1.083	1.089	1.075
CH_2	1.083	1.077	1.083	1.069
CO	1.203	1.203	1.202	1.194
∠HCH	119.3	120.1	119.5	120.0
∠HCC	120.4	120.0	120.5	120.2
∠CCO	126.6	126.2	126.7	128.6
		transition state		
CC	2.311	2.312	2.000	2.000
CH_1	1.084	1.079	1.085	1.075
CH_2	1.082	1.077	1.082	1.069
CO	1.147	1.148	1.162	1.150
∠HCH	132.8	132.3	126.4	126.1
∠HCC	115.1	113.6	117.1	117.7
∠CCO	115.3	113.8	118.5	118.4

[a] Reference 6. [a] See the caption of Table 1 for the notation.

minimum energy profiles obtained with the MRMP::B3LYP and CASSCF::B3LYP functions for the S_0 and T_1 states (shown as cross symbols). It is seen that the latter agrees almost exactly with the minimum energy profiles of the high-level theory (solid line), which is ensured by the property in eq 6. As another test, we calculated the stationary points and normal frequencies on the dual-level PES, which are summarized in Tables 1−3. Here, the stationary points on the (original) CASSCF PES are determined by using analytical gradients, while the stationary points on the MRMP PES are obtained from a local least-squares fit.[6] Tables 1 and 2 show that the agreement between the dual-level PESs and the underlying CASSCF and MRMP PESs is satisfactory considering the limited accuracy of the B3LYP method. As for normal frequencies, we see that the agreement is better for high-frequency modes while it is slightly worse for low-frequency modes. To improve the accuracy, one could employ a more complicated functional form for the dual-level potential. However, we did not enter this complexity and instead utilized the simple functional form in eq 3.

II.B. Propagation of ab Initio Trajectory on the Seam Surface. As mentioned in the Introduction, we assume a dynamical model in which the molecule stays for a long time

Table 3. Normal Mode Frequencies (in cm^{-1}) at the Equilibrium and TS Geometries on the T_1 Surface[a]

	MRMP(DL)	MRMP[a]	CASSCF(DL)	CASSCF
		equilibrium geometry		
CC-str	992	911	1009	950
asym-CH-str	3268	3355	3268	3419
sym-CH-str	3123	3188	3123	3258
CO-str	1785	1679	1789	1832
CH$_2$-scissor	1464	1418	1468	1548
CH$_2$-rock	1067	1019	1101	1098
CH$_2$-wag	786	727	785	687
CCO-bend	453	455	451	492
torsion	396	337	394	386
		transition state		
CC-str	339i	328i	513i	556i
asym-CH-str	3369	3431	3350	3428
sym-CH-str	3144	3162	3146	3235
CO-str	2119	2060	2009	2014
CH$_2$-scissor	1136	1123	1219	1348
CH$_2$-rock	390	344	634	555
CH$_2$-wag	264	308	403	427
CCO-bend	203	184	305	286
torsion	147	108	191	175

[a] Reference 6. [a] See the caption of Table 1 for the notation.

on the S_0 surface prior to the $S_0 \rightarrow T_1$ intersystem crossing. This is based on the observation[11,12] that the nonadiabatic transition probability from the S_1 to S_0 surface is on the order of 10^{-2}, while that from the S_0 to T_1 surface (via spin−orbit coupling) is on the order of 10^{-5}. We thus expect that the molecule undergoes a large number of vibrations on the S_0 surface, and thus intramolecular vibrational energy redistribution (IVR) proceeds. On the basis of this consideration, we assume that the S_0 species is described by the microcanonical distribution

$$f_{S_0}(\mathbf{r}, \mathbf{p}) = \delta[E - H_{S_0}(\mathbf{r}, \mathbf{p})] \tag{10}$$

where $(\mathbf{r}, \mathbf{p})$ are the coordinates and momenta of the molecule, $H_{S_0}(\mathbf{r}, \mathbf{p})$ is the Hamiltonian of the S_0 species, and E is the total energy. The S_0 species crosses to the T_1 surface via the S_0/T_1 seam surface, which is given by $\sigma(\mathbf{r}) = 0$ with

$$\sigma(\mathbf{r}) = U_{S_0}(\mathbf{r}) - U_{T_1}(\mathbf{r}) \tag{11}$$

In this paper, we assume that the surface hopping occurs precisely on the seam surface (i.e., the weak-coupling limit of the intersystem crossing). This indicates that the phase space points crossing to the T_1 surface are characterized by the conditional microcanonical distribution on the seam surface

$$f_{seam}(\mathbf{r}, \mathbf{p}) \propto \delta[E - H_{S_0}(\mathbf{r}, \mathbf{p})]\, \delta[U_{S_0}(\mathbf{r}) - U_{T_1}(\mathbf{r})] \tag{12}$$

(see Appendix A for more rigorous definitions). Our strategy here is to first statistically sample the $S_0 \rightarrow T_1$ crossing points from the seam distribution in eq 12 and then propagate them on the T_1 surface. In this paper, we perform the first task by running a constrained trajectory on the seam surface via the use of a SHAKE-like method. In usual molecular-dynamics

(MD) simulations, the SHAKE method is used to constrain geometric coordinates such as bond lengths. In the present case, we wish to constrain the energy gap between the S_0 and T_1 surfaces. However, if the original SHAKE method is used for this purpose, the calculation becomes quite expensive because it involves iterative solution of $\sigma(\mathbf{r}) = 0$ at every MD step [note that the calculation of $\sigma(\mathbf{r})$ in eq 11 requires ab initio calculation of S_0 and T_1 potential energies]. To avoid this, we consider developing an approximate yet more efficient version of the SHAKE method. In the absence of the constraint, the equation of motion is given by

$$m_i \frac{d^2}{dt^2} \mathbf{r}_i(t) = -\nabla_i U_{S_0}[\mathbf{r}(t)] \equiv \mathbf{F}_i[\mathbf{r}(t)] \tag{13}$$

where $\mathbf{r} = (\mathbf{r}_1, ..., \mathbf{r}_N)$ and $\mathbf{F}_i[\mathbf{r}(t)]$ is the potential force for the S_0 surface. One can discretize eq 13 using the velocity Verlet (VV) integrator

$$\mathbf{v}_i(t + \Delta t/2) = \mathbf{v}_i(t) + \frac{\Delta t}{2m_i} \mathbf{F}_i[\mathbf{r}(t)] \tag{14a}$$

$$\mathbf{r}_i(t + \Delta t) = \mathbf{r}_i(t) + \mathbf{v}_i(t + \Delta t/2)\Delta t \tag{14b}$$

$$\mathbf{v}_i(t + \Delta t) = \mathbf{v}_i(t + \Delta t/2) + \frac{\Delta t}{2m_i} \mathbf{F}_i[r(t + \Delta t)] \tag{14c}$$

where the three steps are evaluated sequentially. Given that the system is ergodic at total energy E, the VV integrator in eq 14 produces the microcanonical distribution in eq 10. In the presence of the constraint $\sigma(\mathbf{r}) = 0$, the equation of motion is given by

$$m_i \frac{d^2}{dt^2} \mathbf{r}_i(t) = \mathbf{F}_i[\mathbf{r}(t)] - \lambda(t)\nabla_i\sigma[\mathbf{r}(t)] \tag{15}$$

where the second term represents the constraint force and $\lambda(t)$ is the Lagrange multiplier. The corresponding VV integrator reads[15,16]

$$\mathbf{v}_i(t + \Delta t/2) = \mathbf{v}_i(t)$$
$$+ \frac{\Delta t}{2m_i}\{\mathbf{F}_i[\mathbf{r}(t)] - \lambda_R\nabla_i\sigma[\mathbf{r}(t)]\} \tag{16a}$$

$$\mathbf{r}_i(t + \Delta t) = \mathbf{r}_i(t) + \mathbf{v}_i(t + \Delta t/2)\Delta t \tag{16b}$$

$$\mathbf{v}_i(t + \Delta t) = \mathbf{v}_i(t + \Delta t/2) + \frac{\Delta t}{2m_i}\{\mathbf{F}_i[r(t + \Delta t)]$$
$$- \lambda_V\nabla_i\sigma[\mathbf{r}(t + \Delta t)]\} \tag{16c}$$

where λ_R and λ_V are discretized analogs of $\lambda(t)$. The original SHAKE method determines the λ_R by requiring that the constraint condition is satisfied exactly at time $t + \Delta t$, i.e.,

$$\sigma[\mathbf{r}(t + \Delta t; \lambda_R)] = 0 \tag{17}$$

This is an implicit equation for the unknown λ_R, which is solved via iteration in the original SHAKE method. This iterative solution requires repeated evaluation of σ, which is

expensive in the present case. We thus solve eq 17 approximately by expanding $\sigma[\mathbf{r}(t + \Delta t)]$ up to the first order in terms of $\mathbf{r}(t + \Delta t) - \mathbf{r}(t)$ about $\mathbf{r}(t)$, namely

$$
\begin{aligned}
\sigma[\mathbf{r}(t + \Delta t)] \simeq {} & \sigma[\mathbf{r}(t)] \\
& + \sum_i \nabla_i \sigma[\mathbf{r}(t)] \cdot \Delta t \Big\{ \mathbf{v}_i^u(t + \Delta t/2) \\
& - \frac{\Delta t}{2m_i} \lambda_R \nabla_i \sigma[\mathbf{r}(t)] \Big\} \equiv 0
\end{aligned} \tag{18}
$$

where $\mathbf{v}_i^u(t + \Delta t/2)$ is the unconstrained velocity at $t + \Delta t/2$

$$
\mathbf{v}_i^u(t + \Delta t/2) = \mathbf{v}_i(t) + \frac{\Delta t}{2m_i} \mathbf{F}_i[\mathbf{r}(t)] \tag{19}
$$

The above approximation gives

$$
\lambda_R = \frac{\sigma[\mathbf{r}(t)] + \Delta t \sum_i \nabla_i \sigma[\mathbf{r}(t)] \cdot v_i^u(t + \Delta t/2)}{(\Delta t^2/2) \sum_i \{\nabla_i \sigma[\mathbf{r}(t)]\}^2/m_i} \tag{20}
$$

It is important to note that $\sigma[\mathbf{r}(t)]$ in eq 20 should be retained explicitly in order to allow small fluctuations of $\sigma[\mathbf{r}(t)]$ while suppressing its systematic drift from zero. On the other hand, the second Lagrange multiplier λ_V in eq 16 can be determined exactly by requiring the velocity constraint at $t + \Delta t$:

$$
\begin{aligned}
\dot\sigma[\mathbf{r}(t + \Delta t)] = {} & \sum_i \nabla_i \sigma[\mathbf{r}(t + \Delta t)] \cdot \Big\{ \mathbf{v}_i^u(t + \Delta t) \\
& - \frac{\Delta t}{2m_i} \lambda_V \nabla_i \sigma[\mathbf{r}(t + \Delta t)] \Big\} \equiv 0
\end{aligned} \tag{21}
$$

where $\mathbf{v}_i^u(t + \Delta t)$ is the unconstrained velocity at $t + \Delta t$

$$
\mathbf{v}_i^u(t + \Delta t) = \mathbf{v}_i(t + \Delta t/2) + \frac{\Delta t}{2m_i} \mathbf{F}_i[\mathbf{r}(t + \Delta t)] \tag{22}
$$

The obtained λ_V is

$$
\lambda_V = \frac{\sum_i \nabla_i \sigma[\mathbf{r}(t + \Delta t)] \cdot \mathbf{v}_i^u(t + \Delta t)}{(\Delta t/2) \sum_i \{\nabla_i \sigma[\mathbf{r}(t + \Delta t)]\}^2/m_i} \tag{23}
$$

With the above procedure, one can propagate a constrained trajectory with only a single evaluation of σ per MD step. Since σ in eq 11 is obtained from the S_0 and T_1 potential energies, the computational cost for propagating a constrained trajectory is identical to that of an unconstrained trajectory.

Before proceeding, it is useful to make some comments on the above integrator. First, because λ_R is evaluated only approximately, the discretization error is slightly greater than in the case where λ_R is evaluated exactly (see below for comparison). To reduce the error, we additionally perform a velocity scaling at each MD step so that the energy is conserved exactly. Second, we note that the constrained trajectory gives the following phase-space distribution:[22,23]

$$
f_{shake}(\mathbf{r}, \mathbf{p}) \propto \delta[E - H_{S_0}]\delta[\sigma]\delta[\dot\sigma] \tag{24}
$$

The $f_{shake}(\mathbf{r},\mathbf{p})$ above differs from $f_{seam}(\mathbf{r},\mathbf{p})$ in eq 12 in that the velocity constraint factor $\delta[\dot\sigma]$ is present. The latter factor reflects the fact that the velocity of a constrained trajectory is
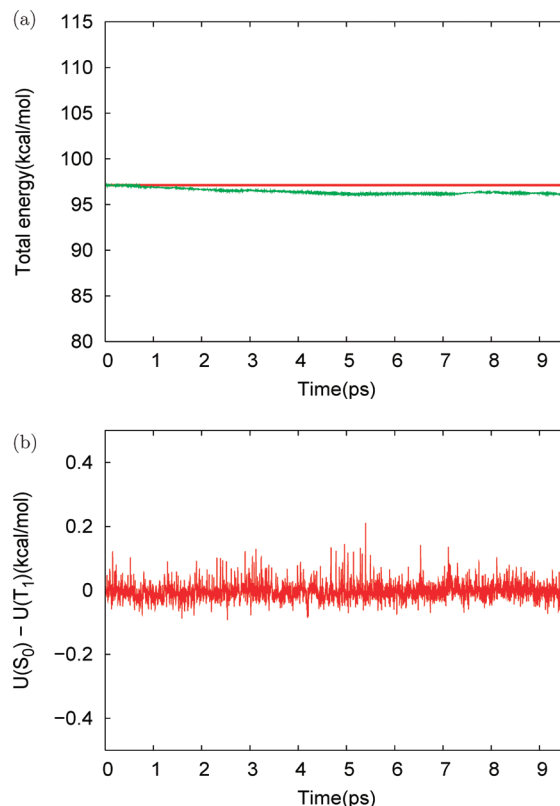

Figure 5. (a) Total energy of the seam trajectory as a function of time. When the velocity scaling is not applied, the total energy exhibits a slight drift on the order of 0.1 kcal/mol/ps (green line). With velocity scaling applied, the total energy is conserved exactly (red line). (b) The difference between the S_0 and T_1 potential energies, $\sigma = U_{S_0} - U_{T_1}$, calculated along the seam trajectory.

always tangent to the constraint surface, $\sigma(\mathbf{r}) = 0$. Since we are interested in generating $f_{seam}(\mathbf{r},\mathbf{p})$ rather than $f_{shake}(\mathbf{r},\mathbf{p})$, we need to correct for the above difference. This correction can be made in a manner similar to the bluemoon sampling method[23] (see Appendix A). Third, since we are running a classical trajectory for statistical sampling, the so-called quasi-ergodicity[24] may become a problem. To examine this, we performed periodic resampling of velocities during the trajectory propagation. We find that the results obtained with velocity resampling are very similar to those without velocity resampling, which indicates that the quasi-ergodicity problem is not of serious concern for the present system (we note, however, that for low-energy systems such as van der Waals clusters, statistical sampling via classical trajectories can be more problematic; see ref 24).

Using the SHAKE-like method described above, we propagated a constrained trajectory on the seam surface with a time step of 0.5 fs up to a maximum time of 10 ps. Figure 5a displays the time evolution of the total energy with or without velocity scaling applied at each MD step. We see that the energy drift is as small as 0.1 kcal/ps even without velocity scaling applied (green line). Nevertheless, in the following calculations we always apply the velocity scaling to conserve the total energy exactly. Figure 5b displays the time evolution of the energy gap $\sigma(\mathbf{r}) = U_{S_0} - U_{T_1}$. As seen, the $\sigma(\mathbf{r})$ remains close to zero with a maximum deviation of 0.2 kcal/mol. This indicates that the first-order expansion of $\sigma(\mathbf{r})$ in eq 18 does not introduce a significant error into the trajectory propagation. In the next section, we will utilize

2512

dx.doi.org/10.1021/ct200367y | J. Chem. Theory Comput. 2011, 7, 2507–2519

the above approximate integrator to obtain the conditional microcanonical distribution on the seam surface.

III. RESULTS AND DISCUSSION

In the following, we consider three simulation conditions regarding the type of dual-level PES and the total energy of the system. First, under the "MRMP" simulation condition, we study the dynamics using the MRMP::B3LYP PES at a total energy of 97.1 kcal/mol (as measured from the S_0 minimum). The latter total energy is equal to the dissociation threshold on the T_1 surface at the MRMP2 level (81.8 kcal/mol) plus the sum of zero-point energies at the T_1 TS geometry (15.3 kcal/mol). The above condition is intended to match most closely with the experimental condition[2] (we recall that the steplike structure in $k(E)$ was observed in the T_1 dissociation threshold region). In the following, we will refer to the total energy minus the potential energy of the TS geometry as the TS excess energy. With this definition, the excess energy in the MRMP condition is simply equal to the ZPE at the TS geometry. Second, in the "CASSCF" simulation condition we study the dynamics using the CASSCF::B3LYP PES at a total energy of 97.1 kcal/mol (which is identical to that in the MRMP condition). The TS excess energy under the CASSCF condition (28.5 kcal/mol) is significantly larger than that under the MRMP condition (15.3 kcal/mol). This is because the dissociation barrier height on the T_1 surface is considerably small at the CASSCF level (16.3 kcal/mol) compared to that at the MRMP level (29.3 kcal/mol). Third, under the "CASSCF(K)" simulation condition, we study the dynamics using the CASSCF::B3LYP PES at a total energy of 82.8 kcal/mol. This condition is intended to match most closely with the surface-hopping study by Kaledin et al.,[12] where the total energy is set equal to the $S_0 \rightarrow S_1$ vertical excitation at the SA-CASSCF level. The TS excess energy under the CASSCF(K) condition is 14.2 kcal/mol, which is again close to the experimental condition.

III.A. Statistical Distribution on the Seam Surface. Figure 6 displays the statistical distribution of (R, U_{T_1}) on the seam surface obtained from the constrained trajectory calculation (section II.B). Here, R is the CC bond length and U_{T_1} denotes the T_1 potential energy as measured from the T_1 equilibrium geometry. Under the MRMP simulation condition [Figure 6a], the value of U_{T_1} is broadly distributed up to 40 kcal/mol, which roughly corresponds to the total energy of the trajectory (as measured from the T_1 minimum). The CC bond length is distributed in the range $1.25 < R < 1.85$ Å, which is essentially localized in the T_1 reactant region. The sampled values of U_{T_1} are generally greater than the corresponding value of the T_1 minimum energy profile [Figure 4b] at the same value of R. This is because the internal coordinates other than R may be excited vibrationally on the seam surface. At the MRMP level, the stationary values of R for the T_1 minimum, S_0/T_1 MSX, and T_1 TS geometries are 1.46, 1.52, and 2.31 Å, respectively. Since the value of R is distributed only up to 1.85 Å, it follows that the phase-space points on the seam surface are located in the vicinity of the S_0/T_1 MSX point ($R = 1.5$ Å), and the seam trajectory hardly accesses the TS region ($R = 2.3$ Å). Figure 6b displays the distribution of (R, U_{T_1}) obtained with the CASSCF simulation condition. As seen, the overall shape of the distribution is rather close to that in the MRMP condition. This is probably because the topography of the T_1 PES in the reactant region ($R < 1.75$) is very similar between the CASSCF and MRMP results, despite the fact that they are significantly different in the TS and product region
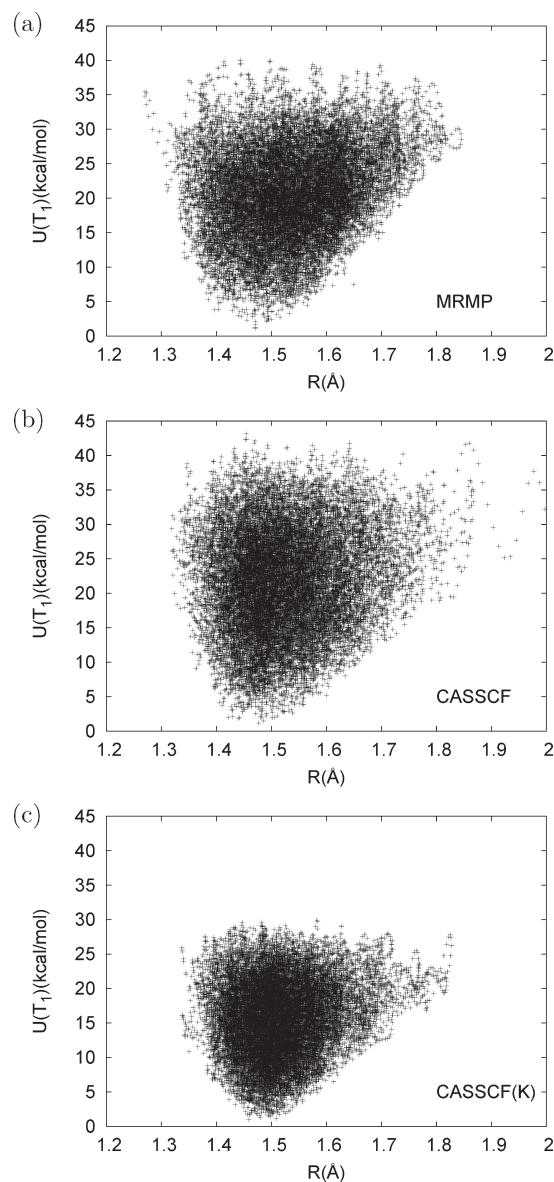
Figure 6. Statistical distribution of (R, U_{T_1}) on the S_0/T_1 seam surface calculated under the MRMP, CASSCF, and CASSCF(K) simulation conditions. R is the CC bond length, and U_{T_1} is the T_1 potential energy measured from the T_1 minimum.

[see Figure 4b]. Under the CASSCF condition, we frequently observed that the seam trajectory escaped from the reactant region and dissociated to the product region. An example of such a trajectory is shown in Figure 4b with $R > 1.9$ Å. This is to be expected because the TS excess energy under the CASSCF condition is very large (28.5 kcal/mol) compared to that under the MRMP condition (15.3 kcal/mol). Another factor that facilitates the dissociation is the closeness of the TS geometry at the CASSCF level to the reactant region. This is seen from the stationary values of R at the CASSCF level for the T_1 minimum, S_0/T_1 MSX, and T_1 TS points, which are 1.47, 1.53, and 2.00 Å, respectively. Figure 6c displays the result for the CASSCF(K) condition. Since the total energy under the latter condition is smaller by 14 kcal/mol than that in the MRMP condition, the value of U_{T_1} is distributed only up to 30 kcal/mol (as measured from the T_1 minimum). Figure 6c shows that the seam distribution
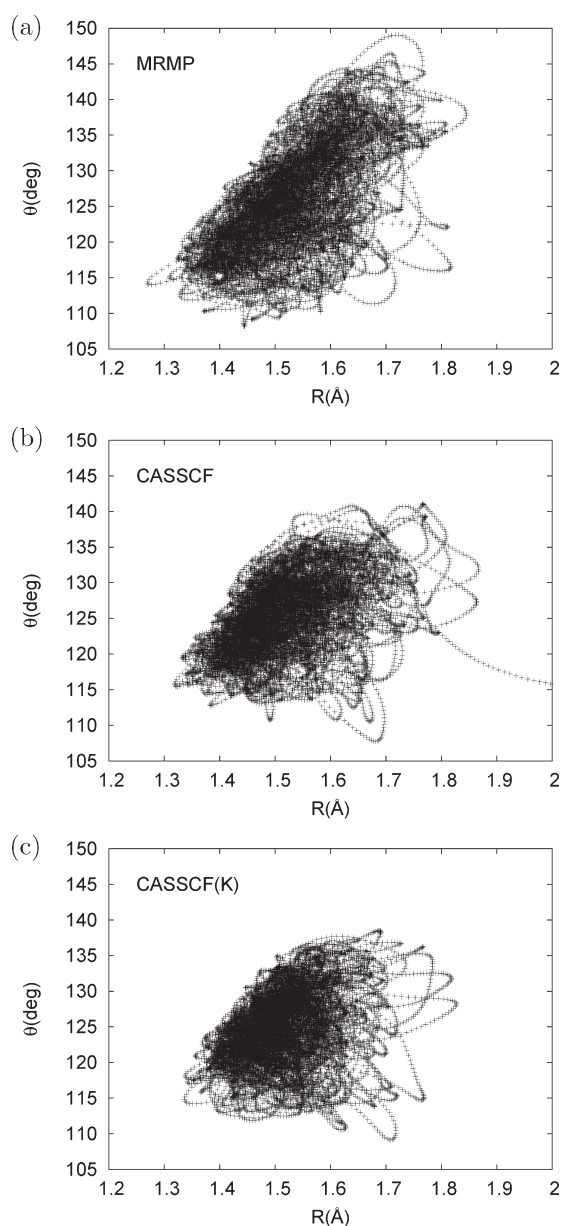
Figure 7. Statistical distribution of (R,θ) on the S_0/T_1 seam surface calculated under the MRMP, CASSCF, and CASSCF(K) simulation conditions. R is the CC bond length, and θ is the CCO bending angle.

Figure 8. Two-dimensional potential map as a function of (R,θ) calculated with the MRMP::B3LYP potential functions. Panel b is obtained by optimizing the internal coordinates other than (R,θ) on the T_1 PES. Panel a displays the S_0 potential energy calculated with the same coordinate set as used in panel a. Panel c displays the energy difference between panels a and b. The red, thick line in panel c is the seam line defined by $U(S_0) = U(T_1)$. The symbols M′, M, and TS indicate the location of the S_0 minimum, T_1 minimum, and T_1 TS geometries, respectively. Energies are in kcal/mol and measured from the S_0 minimum.

is again localized in the reactant region, exhibiting no dissociating trajectory. This indicates that the region $R > 1.9$ Å has little contribution to the conditional microcanonical distribution on the seam and that the $S_0 \rightarrow T_1$ surface crossing occurs mainly in the T_1 reactant region.

Figure 7 displays the distribution of (R,θ) obtained under the individual simulation conditions. Here, θ denotes the CCO bending angle (see Figure 2). Under the MRMP condition, the θ is widely distributed in the range $110° < \theta < 145°$ and roughly centered at the S_0/T_1 MSX point ($R = 1.490$ Å and $\theta = 124.5°$). Under the CASSCF and CASSCF(K) conditions, the distribution of θ is somewhat more localized compared to the MRMP condition. In Figure 7, the values of θ tend to increase with R, which indicates that the molecule assumes a more linear geometry of the CCO moiety as R is increased. This trend is in
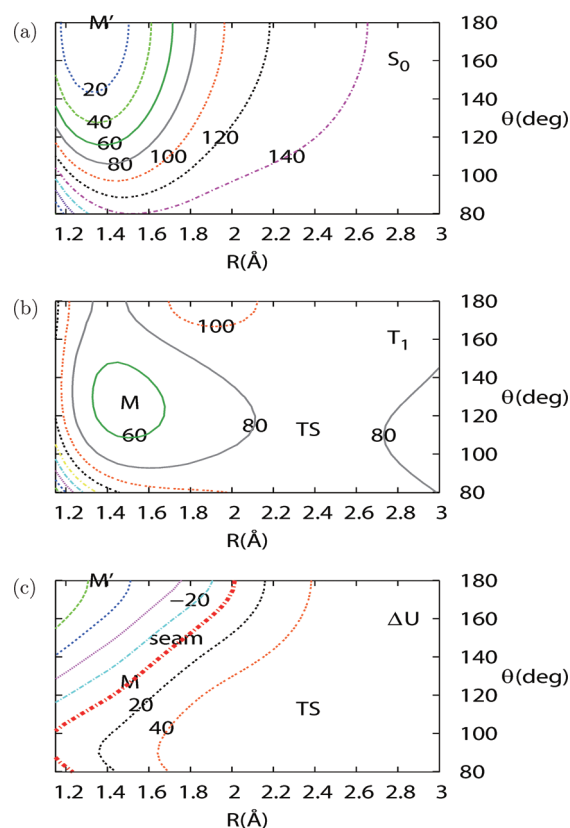
qualitative agreement with the previous study by Cui and Morokuma,[11] which obtained partially optimized geometries on the seam surface at several values of R. To obtain further insight, we display in Figure 8 the two-dimensional map of the S_0 and T_1 surfaces at the MRMP level. Here, the T_1 potential map in panel b is obtained by adiabatically optimizing the internal coordinates other than (R,θ) on the T_1 PES, whereas the S_0 potential map in panel a was obtained by using the same coordinate set as that used in panel b. Those potential maps indicate that the S_0 surface favors a more linear geometry with $\theta \simeq 180°$, while the T_1 state favors a more bent geometry with $\theta \simeq 130°$. The energy difference between the two potential maps is plotted in panel c, which exhibits a seam line running from $R \simeq 1.2$ Å and $\theta \simeq 100°$ to $R \simeq 2.0$ Å and $\theta \simeq 180°$. A comparison between Figures 7 and Figure 8c shows that the phase-space points are roughly centered around the seam line thus obtained.

Figure 9 displays the distribution of (R,ϕ) on the seam surface. We recall that the torsional angle ϕ is $0°$ for planar Cs−II symmetry and $90°$ for nonplanar Cs−I symmetry. Previous studies have shown[7,11] that the important geometries such as the T_1 minimum and the S_0/T_1 MSX point are of planar Cs−II symmetry. Nevertheless, we see from Figure 9 that ϕ is widely
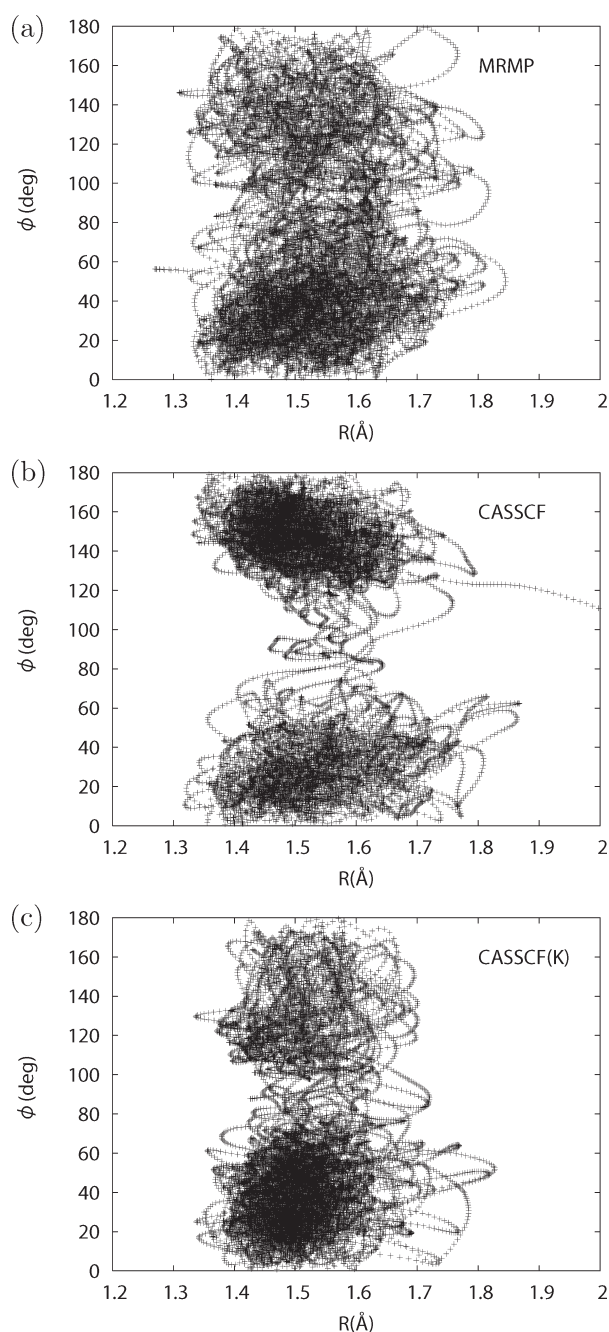
Figure 9. Statistical distribution of (R,ϕ) on the S_0/T_1 seam surface calculated with the MRMP, CASSCF, and CASSCF(K) simulation conditions. R is the CC bond length, and ϕ is the torsional angle.
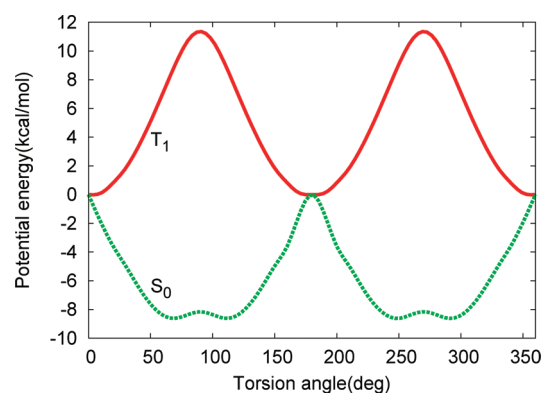

Figure 10. Potential energy profiles of the S_0 and T_1 surfaces as a function of the torsional angle ϕ obtained with the MRMP::B3LYP potential functions. Internal coordinates other than (R,θ) are optimized at each value of ϕ. The values of R and θ are fixed at the S_0/T_1 MSX geometry ($R = 1.491$ Å and $\theta = 124.5°$). Note that the minima of the S_0 potential are slightly off the Cs−I symmetry because θ is frozen at the MSX geometry.
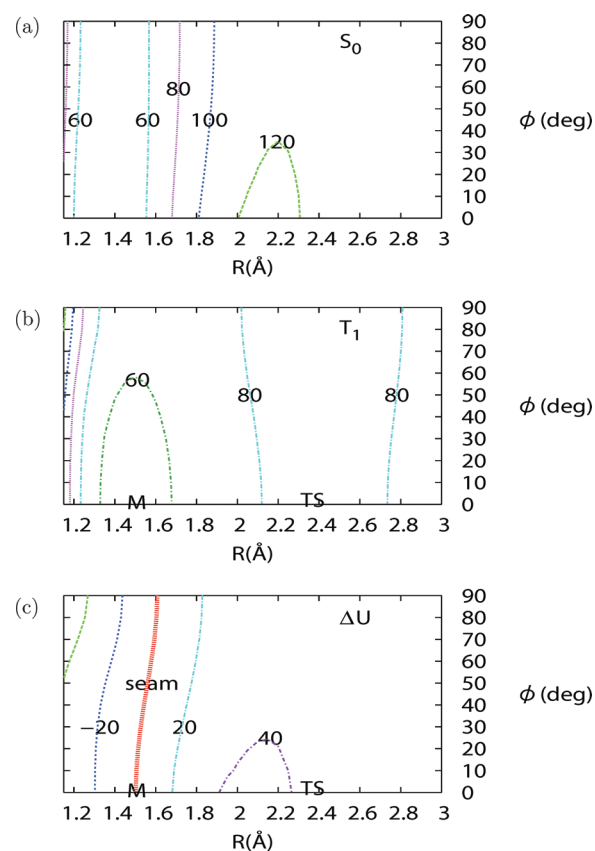

Figure 11. Two-dimensional potential map as a function of (R, ϕ) calculated with the MRMP::B3LYP potential functions. See the caption of Figure 8 for computational details.

distributed over $0 < \phi < 180°$, indicating that the molecule is not limited to planar Cs−II geometries upon surface crossing. A closer look at Figure 9 reveals that the distribution of ϕ is bimodal and centered at around 40° and 140°, which are of neither Cs−I nor Cs−II symmetry. Several factors may be responsible for the above observation. First, the distribution on the seam tends to get delocalized by the effect of kinetic energy. Second, since Figure 9 is obtained by projecting out the internal coordinates other than (R,ϕ), the two-dimensional distribution reflects the accessible number of states (or phase-space volume) of the projected coordinates at individual values of (R,ϕ). Third, the ϕ dependences of the S_0 and T_1 PESs are rather different. To illustrate this,

we plot in Figure 10 the adiabatically optimized potential curves as a function of ϕ for the S_0 and T_1 states [here, the values of (R,θ) are fixed at the S_0/T_1 MSX geometry]. As seen, the equilibrium values of ϕ are different between the S_0 and T_1 states, which seems most responsible for the broad distribution of ϕ in Figure 9 . For further information, Figure 11 displays the

2515

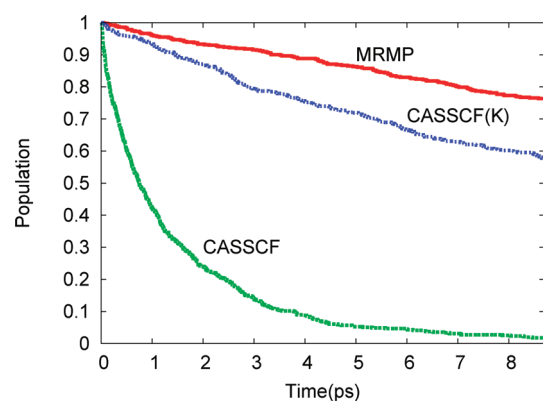dx.doi.org/10.1021/ct200367y |*J. Chem. Theory Comput.* 2011, 7, 2507–2519

Figure 12. Time-dependent survival probability $P_{surv}(t)$ on the T_1 surface calculated under the MRMP, CASSCF, and CASSCF(K) simulation conditions.

two-dimensional map of the S_0 and T_1 potentials as a function of (R, ϕ). The seam line runs from around $R = 1.5$ Å and $\phi = 0°$ to $R = 1.6$ Å and $\phi \simeq 90°$, and it is again seen that the phase-space points are distributed roughly around the seam line.

III.B. Dissociation Rate on the T_1 Surface. We now calculate the dissociation rate by propagating a number of trajectories on the T_1 surface. To do so, we assume the weak-coupling limit of intersystem crossing, and accordingly a trajectory is propagated adiabatically on the T_1 surface.[25] To prepare the initial state of the trajectory, we picked up 500 points randomly from the seam distribution obtained in section III.A, followed by an appropriate resampling of velocities (see Appendix A). The initial phase-space points thus obtained were propagated on the T_1 surface until they dissociated or the integration time exceeded 9 ps. The progress of the reaction was monitored by calculating the time-dependent survival probability defined by

$$P_{surv}(t) = \frac{\langle |v_\perp| P_{NA}(v_\perp) \, \Theta(R^\ddagger - R_t) \rangle_{seam}}{\langle |v_\perp| P_{NA}(v_\perp) \rangle_{seam}} \qquad (25)$$

Here, $\langle...\rangle_{seam}$ denotes an ensemble average over the initial phase-space points on the seam surface, $\Theta(R^\ddagger - R_t)$ is the Heaviside step function, and $v_\perp$ is the component of the velocity vector normal to the seam surface (see Appendix A for more details). The $P_{NA}(v_\perp)$ in eq 25 is the nonadiabatic transition probability calculated with the Landau−Zener formula:[26−28]

$$P_{NA}(v_\perp) = 1 - \exp\left[-\frac{2\pi}{\hbar} \frac{H_{SO}^2}{|\Delta F v_\perp|}\right] \qquad (26)$$

Here, H_{SO} is the S_0−T_1 spin−orbit coupling and ΔF is the normal component of the difference gradient vector $\nabla(U_{S0} - U_{T1})$. In this paper, we approximated H_{SO} to be constant and set it to 43 cm^{-1} (calculated at the CASSCF level). By fitting the survival probability to a single exponential form

$$P_{surv}(t) \simeq \exp(-kt) \qquad (27)$$

we estimated the dissociation rate k and the associated lifetime $\tau = 1/k$ on the T_1 surface.

Figure 12 displays the survival probability thus obtained for individual simulation conditions. Table 4 lists the corresponding dissociation rate k and lifetime τ. Under the CASSCF conditions, the dissociation is very fast, with $\tau = 1.4$ ps, which is clearly due to the large excess energy (28.5 kcal/mol) at the TS geometry.

Table 4. Dissociation Rate k on the T_1 Surface (in ps^{-1}) Obtained from the Trajectory Calculations[a]

	MRMP	CASSCF	CASSCF(K)
RRKM ($\hbar = 1.00$)	0.0017 (590)	2.59 (0.39)	0.057 (17.5)
RRKM ($\hbar = 0.50$)	0.0462 (21.6)	3.48 (0.29)	0.223 (4.5)
RRKM ($\hbar = 0.25$)	0.0656 (15.2)	3.69 (0.27)	0.353 (2.8)
RRKM ($\hbar = 0.10$)	0.0715 (14.0)	3.75 (0.26)	0.391 (2.6)
trajectory calcd	0.0276 (36.2)	0.710 (1.4)	0.0677 (14.8)

[a] The RRKM rates obtained with various values of $\hbar$ (in atomic units) are also shown. The corresponding lifetime $\tau = 1/k$ (in ps) is given in parentheses.

Under the MRMP and CASSCF(K) conditions, the reaction proceeds much slower than under the CASSCF condition. The calculated values of τ are 36.2 ps for the MRMP condition and 14.8 ps for the CASSCF(K) condition. A critical observation here is that the latter values are significantly greater than that obtained in the previous trajectory study by Kaledin et al.[12] In the latter study, half the trajectories dissociated within ∼120 fs after making a transition to the T_1 surface (or within ∼260 fs after $S_0 \rightarrow S_1$ vertical excitation). This means that the dissociation rate under the MRMP and CASSCF(K) conditions are about 2 orders of magnitude smaller than obtained in ref 12. This is somewhat surprising because the CASSCF(K) condition has the same total energy and level of electronic structure theory as employed in ref 12. The marked difference in the dissociation rates is thus attributed to the different ways of preparing the T_1 trajectories. Specifically, in ref 12, the parent trajectory was first evolved on the S_1 surface (after initial vertical excitation), and it was allowed to branch every time the S_1 surface crossed the S_0 surface. At the branching point, the parent trajectory continued to be propagated on the S_1 surface, whereas the child trajectory started to evolve on the S_0 surface. A similar procedure was applied to obtain child trajectories on the T_1 surface. A critical point here is that the propagation time of the S_0 trajectory was rather short (up to ∼300 fs), and the number of the S_0 and T_1 trajectories was relatively small (a total of 10). This indicates that the T_1 trajectories may be affected considerably by the short-time dynamics of the S_0 trajectories after vertical excitation. Since the molecule is vibrationally excited in the CC stretching and CCO bending modes upon vertical excitation, the dissociation may be facilitated to some extent by selective excitation of those vibrational modes (we recall here that the CC stretch plays the role of reaction coordinate for this system). By contrast, in the present calculation, we have assumed a vibrational equilibrium on the S_0 surface and propagated T_1 trajectories starting from the conditional microcanonical distribution on the seam surface. We expect that the above different ways of preparing the T_1 trajectories are mainly responsible for the different rates obtained in the present study and in ref 12.

Another question to be asked here is whether the dissociation dynamics on the T_1 surface may be regarded as statistical or not. This is because the previous rate calculations[2,3,6] relied on statistical rate theories that assume a vibrational equilibrium on the T_1 surface. Those calculations are thus reliable only when the IVR on the T_1 surface proceeds considerably prior to the dissociation. To examine this, we have calculated the RRKM rate for the T_1 dissociation. Here, it should be noted that the usual RRKM rate refers to a *quantum mechanical* unimolecular reaction rate, which cannot be compared directly to the present classical

trajectory results. Rather, we need to calculate a *classical mechanical* reaction rate assuming a vibrational equilibrium on the T_1 surface. In this paper, we performed this task by calculating the RRKM rate with decreasing values of $\hbar$ (see Appendix B for details), the results of which are summarized in Table 4. We see from this table that the RRKM rate is fairly converged with $\hbar = 0.1$ (in atomic units), which we regard as the "classical" transition state theory (TST) rate, and it is seen that the latter is in reasonable agreement with the present classical trajectory result. The deviation between the trajectory and classical RRKM results is within a factor of 3 for the MRMP condition and 6 for the CASSCF(K) condition. A possible reason for the deviation is the so-called recrossing effect of trajectories over the potential barrier. However, we expect that the latter effect is minor for the present system because the T_1 surface is rather separable in the TS region.[6] A more plausible reason for the above deviation is an inefficient IVR on the T_1 surface. Figure 11 indicates that the vibrational coupling between R and ϕ coordinates is fairly small, which may lead to inefficient energy transfer from ϕ to R and hence the underestimation of the rate in the trajectory calculation (recall that R plays the role of reaction coordinate, and thus its activation is essential for the dissociation). Nevertheless, since the discrepancy between the trajectory and classical RRKM results is not particularly large (within a factor of 3 in the MRMP condition), the T_1 dissociation seems to be rather statistical (at least not highly nonstatistical), given that the trajectory is initiated from the conditional microcanonical distribution on the seam surface.

IV. CONCLUDING REMARKS

In this paper, we have revisited the still unresolved problem of triplet ketene regarding the stepwise structure in the observed rate.[2] In particular, we focused on whether the T_1 dissociation may be regarded as statistical, because this has been the fundamental assumption of the previous rate calculations.[2,3,6] To examine this, we have introduced the assumption of a vibrational equilibrium on the S_0 surface and calculated the dissociation rate by running T_1 trajectories from the seam surface. The main results obtained are the following: (1) The $S_0 \rightarrow T_1$ crossing points are located mainly in the T_1 reactant region. (2) The T_1 dissociation rate is significantly smaller than the previous surface-hopping result by Kaledin et al.[12] (3) The present trajectory result agrees reasonably well with the classical RRKM result. As noted above, the discrepancy between the present study and ref 12 is probably due to the different ways of preparing the T_1 trajectories, rather than the different levels of electronic structure theory used. This is based on the observation that even under the CASSCF(K) condition there remains a significant difference in the rates between the two calculations. We expect that if a surface-hopping simulation is performed with a very long S_0 trajectory and a sufficient number of T_1 trajectories, the discrepancy between the two studies would probably be reduced.

While we have studied the T_1 dissociation from a statistical point of view, we cannot make further arguments on the possible nonadiabatic effect on the steplike structure in $k(E)$. To investigate the latter, it is desirable that one performs a quantum dynamical nonadiabatic simulation involving S_0 and T_1 states. (Here, we emphasize that the present study as well as the previous one by Kaledin et al.[12] is performed wholly in terms of classical mechanics, except that ZPE was taken into account to define the total energy.) An approach to that end is to introduce a reduced-dimensional model that involves S_0 and T_1 states, which

is the strategy used previously for the adiabatic dynamics on the T_1 surface.[3,6] The multiconfiguration time-dependent Hartree method[29−32] may also be useful for this purpose. An alternative approach is to use a trajectory-based simulation method that includes nuclear quantum effects approximately.[33−36] Application of those methods to the nonadiabatic dynamics of ketene may provide more mechanistic insights into the observed steps in $k(E)$.

■ APPENDIX A: CONDITIONAL MICROCANONICAL DISTRIBUTION ON THE SEAM SURFACE

In this paper, we define the conditional microcanonical distribution on the seam surface as follows:

$$f_{seam}(\mathbf{r}, \mathbf{p}) = \delta(E - T - U_0)\,\delta(\sigma)|\nabla\sigma| \tag{A1}$$

where $\mathbf{r} = (\mathbf{r}_1, ..., \mathbf{r}_N)$ and $\mathbf{p} = (\mathbf{p}_1, ..., \mathbf{p}_N)$ are the coordinates and momenta in mass-weighted coordinates with $\nabla = \partial/\partial\mathbf{r}$, and $T = \mathbf{p}^2/2$ is the kinetic energy of the molecule. Hereafter, we denote the potential energies of the S_0 and T_1 states as $U_0(\mathbf{r})$ and $U_1(\mathbf{r})$, respectively, and σ represents the energy gap

$$\sigma(\mathbf{r}) = U_0(\mathbf{r}) - U_1(\mathbf{r}) \tag{A2}$$

The $|\nabla\sigma|$ in eq A1 is a geometric factor that makes $f_{seam}(\mathbf{r},\mathbf{p})$ invariant to an arbitrary scaling of $\sigma(\mathbf{r})$, namely, $\sigma(\mathbf{r}) \rightarrow \kappa(\mathbf{r})\,\sigma(\mathbf{r})$. For simplicity of discussion, we first consider the following form of the survival probability on the T_1 surface

$$P_{surv}(t) = \langle\Theta(R^{\ddagger} - R_t)\rangle_{seam} \tag{A3}$$

where $\langle\cdots\rangle_{seam}$ is an ensemble average defined by

$$\langle\cdots\rangle_{seam} = \frac{\int d\mathbf{r} \int d\mathbf{p}\, f_{seam}(\mathbf{r}, \mathbf{p})(\cdots)}{\int d\mathbf{r} \int d\mathbf{p}\, f_{seam}(\mathbf{r}, \mathbf{p})} \tag{A4}$$

We evaluate the above average by propagating a constrained trajectory on the seam surface. To do so, we recall that a microcanonical system with a holonomic constraint $\sigma(\mathbf{r}) = 0$ has the following phase-space distribution:[22]

$$f_{shake}(\mathbf{r}, \mathbf{p}) = \delta(E - T - U_0)\,\delta(\sigma)\,\delta(\dot{\sigma})|\nabla\sigma|^2 \tag{A5}$$

A critical difference between $f_{shake}(\mathbf{r},\mathbf{p})$ and $f_{seam}(\mathbf{r},\mathbf{p})$ is that the former includes the velocity constraint, $\dot{\sigma} = \nabla\sigma\cdot\mathbf{v} = 0$, which states that the velocity of the constrained system is always tangential to the constraint surface, $\sigma(\mathbf{r}) = 0$. Note that such a velocity constraint is absent in the ensemble of phase-space points associated with S_0/T_1 intersystem crossing. To account for this difference, it is useful to introduce the position distribution function obtained by integrating over the momenta[37]

$$\tilde{f}_{seam}(\mathbf{r}) = \int d\mathbf{p}\, f_{seam}(\mathbf{r}, \mathbf{p})$$

$$= const \times [E - U_0]^{(n-2)/2}\delta(\sigma)|\nabla\sigma| \tag{A6}$$

$$\tilde{f}_{shake}(\mathbf{r}) = \int d\mathbf{p}\, f_{shake}(\mathbf{r}, \mathbf{p})$$

$$= const \times [E - U_0]^{(n-3)/2}\delta(\sigma)|\nabla\sigma| \tag{A7}$$

2517

dx.doi.org/10.1021/ct200367y |*J. Chem. Theory Comput.* 2011, 7, 2507–2519

where n is the number of degrees of freedom and const represents a constant independent of $(\mathbf{r},\mathbf{p})$. Note that the exponent of $[E - U_0]$ is different by $1/2$ between eqs A6 and A7, which suggests

$$\tilde{f}_{seam}(\mathbf{r}) = const \times [E - U_0]^{1/2} \tilde{f}_{shake}(\mathbf{r}) \tag{A8}$$

The above relation can be used to calculate an ensemble average over $f_{seam}(\mathbf{r},\mathbf{p})$ by sampling $f_{shake}(\mathbf{r},\mathbf{p})$. To do so, we first rewrite the ensemble average in eq A3 as follows:

$$\langle \Theta_t \rangle_{seam} = \frac{\int d\mathbf{r}\, \tilde{f}_{seam}(\mathbf{r}) \langle \Theta_t \rangle_p}{\int d\mathbf{r}\, \tilde{f}_{seam}(\mathbf{r})} \tag{A9}$$

where $\Theta_t \equiv \Theta(R^{\ddagger} - R_t)$, and $\langle \cdots \rangle_p$ represents an average over the momenta defined by

$$\langle \cdots \rangle_p = \frac{\int d\mathbf{p}\, f_{seam}(\mathbf{r}, \mathbf{p}) (\cdots)}{\int d\mathbf{p}\, f_{seam}(\mathbf{r}, \mathbf{p})} \tag{A10}$$

By inserting eq A8 into eq A9, we have

$$\langle \Theta_t \rangle_{seam} = \frac{\langle [E - U_0]^{1/2} \langle \Theta_t \rangle_p \rangle_{shake}}{\langle [E - U_0]^{1/2} \rangle_{shake}} \tag{A11}$$

where $\langle \cdots \rangle_{shake}$ is defined by

$$\langle A(\mathbf{r}) \rangle_{shake} = \frac{\int d\mathbf{r}\, \tilde{f}_{shake}(\mathbf{r})\, A(\mathbf{r})}{\int d\mathbf{r}\, \tilde{f}_{shake}(\mathbf{r})}$$

$$= \frac{\int d\mathbf{r} \int d\mathbf{p}\, f_{shake}(\mathbf{r}, \mathbf{p})\, A(\mathbf{r})}{\int d\mathbf{r} \int d\mathbf{p}\, f_{shake}(\mathbf{r}, \mathbf{p})} \tag{A12}$$

where $A(\mathbf{r})$ is an arbitrary function of $\mathbf{r}$. The above average can be evaluated by running a constrained trajectory $(\mathbf{r}_t, \mathbf{p}_t)$ on the seam surface via use of the SHAKE method:[22]

$$\langle A(\mathbf{r}) \rangle_{shake} \simeq \lim_{T \longrightarrow \infty} \frac{1}{T} \int_0^T dt\, A(\mathbf{r}_t) \tag{A13}$$

In the present case, $A(\mathbf{r})$ is given by $[E - U_0]^{1/2} \langle \Theta_t \rangle_p$ in eq A12. The factor $\langle \Theta_t \rangle_p$ is obtained from an (internal) average over the momenta sampled randomly from a sphere of radius $|\mathbf{p}| = (2(E - U_0))^{1/2}$. (In practice, the latter average can be merged with the trajectory propagation by evaluating Θ_t with random momenta rather than with the current momenta of the trajectory.) We also note that the above sampling procedure is analogous to the bluemoon sampling method.[23] In the latter case, one samples a conditional canonical distribution, $\exp(-\beta H)\, \delta(\sigma)$, while in the present case we sample a conditional microcanonical distribution, $\delta(E - H)\, \delta(\sigma)$.

In section III.B, we defined the survival probability on the T_1 surface by taking account of the transition probability, i.e.

$$P_{surv}(t) = \frac{\langle\langle |v_\perp| P_{NA}(v_\perp)\, \Theta(R^{\ddagger} - R_t) \rangle\rangle_{seam}}{\langle\langle |v_\perp| P_{NA}(v_\perp) \rangle\rangle_{seam}} \tag{A14}$$

The latter expression can be evaluated analogously by rewriting it to

$$P_{surv}(t) = \frac{\langle [E - U_0]^{1/2} \langle |v_\perp| P_{NA}(v_\perp)\, \Theta(R^{\ddagger} - R_t) \rangle_p \rangle_{shake}}{\langle [E - U_0]^{1/2} \langle |v_\perp| P_{NA}(v_\perp) \rangle_p \rangle_{shake}} \tag{A15}$$

and calculating the average $\langle \cdots \rangle_{shake}$ with the SHAKE method.

■ APPENDIX B: RRKM RATE CONSTANT AND ITS CLASSICAL LIMIT

The RRKM rate for the T_1 dissociation, $k(E) = N^{\ddagger}(E)/(2\pi\hbar\rho(E))$, was evaluated via direct count of anharmonic vibrational states. Specifically, we first approximated $\rho(E)$ as

$$\rho(E) \simeq \frac{N_R(E + \Delta E) - N_R(E - \Delta E)}{2\Delta E} \tag{B1}$$

where $N_R(E)$ is the number of vibrational states in the T_1 reactant region. The vibrational states at the TS and in the reactant region were obtained approximately as the direct product of one-dimensional eigenstates of the Hamiltonian for individual normal coordinates $\{Q_i\}$:

$$\hat{H}_i = -\frac{\hbar^2}{2} \frac{\partial^2}{\partial Q_i^2} + V_i(Q_i) \tag{B2}$$

where $V_i(Q_i)$ is the one-dimensional section of the T_1 PES in the direction of Q_i. The diagonalization of $\hat{H}_i$ was performed using the discrete variable representation (DVR). For the torsional mode ϕ, we used a hindered-rotor Hamiltonian given by

$$\hat{H}_{tors} = -\frac{\hbar^2}{2I_{eff}} \frac{\partial^2}{\partial \phi^2} + \frac{V_b}{2} [1 - \cos(2\phi)] \tag{B3}$$

where I_{eff} is the effective inertia moment and V_b is the torsional barrier height. Thus, the anharmonicity of the multidimensional PES is approximately taken into account in $\rho(E)$ and $N^{\ddagger}(E)$. The above RRKM calculation was repeated for several different values of $\hbar$ in order to obtain an approximate classical limit ($\hbar \rightarrow 0$). It should be noted that the number of DVR grid points needs to be increased with decreasing $\hbar$. This is because the eigenfunctions becomes more and more oscillatory for small $\hbar$ and also the density of states increases with decreasing $\hbar$. It is also crucial to optimize the way of calculating $N_R(E)$ such that high energy states are not actually included in multidimensional loops, because failure to do so makes the calculation too time-consuming for small $\hbar$.

■ AUTHOR INFORMATION

Corresponding Author

*E-mail: yamamoto@kuchem.kyoto-u.ac.jp.

■ ACKNOWLEDGMENT

2518

dx.doi.org/10.1021/ct200367y | *J. Chem. Theory Comput.* 2011, 7, 2507–2519

■ REFERENCES

(1) Lovejoy, E. R.; Kim, S. K.; Moore, C. B. *Science* **1992**, *256*, 1541.

(2) Kim, S. K.; Lovejoy, E. R.; Moore, C. B. *J. Chem. Phys.* **1995**, *102*, 3202.

(3) Gezelter, J. G.; Miller, W. H. *J. Chem. Phys.* **1996**, *104*, 3546.

(4) Steinfeld, J. I.; Francisco, J. S.; Hase, W. L. *Chemical Kinetics and Dynamics*; Prentice-Hall: Englewood Cliffs, NJ, 1989.

(5) Henriksen, N. E.; Hansen, F. Y. *Theories of Molecular Reaction Dynamics*; Oxford University Press: New York, 2008.

(6) Ogihara, Y.; Yamamoto, T.; Kato, S. *J. Phys. Chem. A* **2010**, *114*, 9981.

(7) King, R. A.; Allen, W. D.; Ma, B.; Schaefer, H. F., III. *Faraday Discuss.* **1998**, *110*, 23.

(8) Ogihara, Y.; Yamamoto, T.; Kato, S. *Chem. Phys. Lett.* **2011**, *511*, 28.

(9) Leu, G.; Huang, C.; Lee, S.; Lee, Y.; Chen, I. *J. Chem. Phys.* **1998**, *109*, 9340.

(10) King, R. A.; Allen, W. D.; Schaefer, H. F., III *J. Chem. Phys.* **2000**, *112*, 5585.

(11) Cui, Q.; Morokuma, K. *J. Chem. Phys.* **1997**, *107*, 4951.

(12) Kaledin, A. L.; Seong, J.; Morokuma, K. *J. Phys. Chem. A* **2001**, *105*, 2731.

(13) Preston, R. K.; Tully, J. C. *J. Chem. Phys.* **1971**, *54*, 4297.

(14) Tully, J. C.; Preston, R. K. *J. Chem. Phys.* **1971**, *55*, 562.

(15) Ryckaert, J.; Ciccotti, G.; Berendsen, H. J. C. *J. Comut. Phys.* **1977**, *23*, 327.

(16) Andersen, H. C. *J. Comut. Phys.* **1983**, *52*, 24.

(17) Dunning, J. T. H. *J. Chem. Phys.* **1989**, *90*, 1007.

(18) Nguyen, K. A.; Rossi, I.; Truhlar, D. G. *J. Chem. Phys.* **1995**, *103*, 5522.

(19) Ruiz-Pernia, J. J.; Silla, E.; Tunon, I.; Marti, S.; Moliner, V. *J. Phys. Chem. B* **2004**, *108*, 8427.

(20) Schmidt, M. W.; Baldridge, K. K.; Boatz, J. A.; Elbert, S. T.; Gordon, M. S.; Jensen, J. H.; Koseki, S.; Matsunaga, N.; Nguyen, K. A.; Su, S.; Windus, T. L.; Dupuis, M.; Montgomery, J. A. *J. Comput. Chem.* **1993**, *14*, 1347.

(21) Granovsky, A. A. Firefly version 7.1.G. http://classic.chem.msu.su/gran/firefly/index.html (accessed July 2011).

(22) Ryckaert, J. P.; Ciccotti, G. *J. Chem. Phys.* **1983**, *78*, 7368.

(23) Carter, E. A.; Ciccotti, G.; Hynes, J. T.; Kapral, R. *Chem. Phys. Lett.* **1989**, *156*, 472.

(24) Calvo, F.; Galindez, J.; Gadea, F. X. *J. Phys. Chem. A* **2002**, *106*, 4145.

(25) Note that the back transfer from the T_1 to the S_0 state is thus totally neglected in this paper. Inclusion of the latter may slightly modify the T_1 dissociation rate because a small fraction of the T_1 trajectories may return to the S_0 state prior to the triplet dissociation.

(26) Landau, L. D. *Phys. Z.* **1932**, *2*, 46.

(27) Zener, C. *Proc. R. Soc. London, Ser. A* **1932**, *137*, 696.

(28) Wittig, C. *J. Phys. Chem. B* **2005**, *109*, 8428.

(29) Manthe, U.; Meyer, H. D.; Cederbaum, L. S. *J. Chem. Phys.* **1992**, *97*, 3199.

(30) Beck, M. H.; Jackle, A.; Worth, G. A.; Meyer, H. D. *Phys. Rep.* **2000**, *324*, 1.

(31) Worth, G. A.; Robb, M. A.; Burghardt, I. *Faraday Discuss.* **2004**, *127*, 307.

(32) Meyer, H.-D.; Gatti, F.; Worth, G. A. *Multidimensional Quantum Dynamics: MCTDH Theory and Applications*; Wiley-VCH: Berlin, 2009.

(33) Garashchuk, S.; Vazhappilly, T. *J. Chem. Phys.* **2009**, *131*, 164108.

(34) Czako, G.; Kaledin, A. L.; Bowman, J. M. *J. Chem. Phys.* **2010**, *132*, 164103.

(35) Czako, G.; Kaledin, A. L.; Bowman, J. M. *Chem. Phys. Lett.* **2010**, *500*, 217.

(36) Yamamoto, T.; Miller, W. H. *J. Chem. Phys.* **2003**, *118*, 2135.

(37) Schranz, H. W.; Nordholm, S.; Nyman, G. *J. Chem. Phys.* **1991**, *94*, 1487.

2519

dx.doi.org/10.1021/ct200367y |*J. Chem. Theory Comput.* 2011, 7, 2507–2519